

PLUG-AND-PLAY FORWARD BACKWARD ALGORITHM TO RESTORE LANDSAT IMAGES AND UNCOVER THE HISTORY OF SURFACE WATERS

Pierre Audisio^{1,2}, Barbara Belletti², Nelly Pustelnik¹

¹Ens de Lyon, CNRS, Laboratoire de Physique, F-69342, Lyon, France.

²Université Jean Monnet, CNRS, UMR 5600 Environnement Ville Société, Saint-Etienne, France.

ABSTRACT

The temporal and spatial analysis of river dynamics is a key factor in studying and understanding human impacts on floodplains. To assess the changes taking place, it is necessary to have high-resolution images with a large spatial coverage and a high temporal revisit frequency over the long term. Satellite imagery meets several of these criteria. This study aims to augment the spatial resolution of Landsat data from 30m to 10m, with an innovative single image super-resolution (SISR) method based on a Plug&Play approach.

Index Terms— Restoration, Plug&Play, remote sensing, neural networks, multispectral data, Landsat-8, Sentinel-2

1. INTRODUCTION

Context - Monitoring river ecosystems is a challenging task due to the complex interactions between ecological and morphological processes. Their complexity lies in their manifestation at multiple spatial scales going from regional or entire watershed to local river sections [1]. These ecosystems are particularly vulnerable to long-term changes driven by anthropogenic pressures, such as urbanization, dam construction, and land use changes [2].

To effectively capture these dynamics, remote sensing offers a powerful solution. However, accurate monitoring requires satellite data with three key characteristics: large spatial coverage, to capture interdependent regions; high spatial resolution, to detect fine-scale features; and short revisit periods, to track temporal changes.

Satellite **hyperspectral** ? imagery is particularly well suited to this issue, due to the possibility of studying **land use**? at specific wavelengths, but also thanks to the availability of open-access data at different spatial resolutions, from 10 to 60 meters depending on the satellite. However, high spatial resolution data (~ 10 m/pixel) has only become available since the early 2000s **with Sentinel satellite**.

Consequently, to capture more detailed and extended temporal information, it is necessary to enhance the resolution of satellite images with lower resolutions, such as those from Landsat.

Contribution - In this study two sources of data are used. Sentinel-2 images, part of the Copernicus project, which started in 2015 [3], and Landsat project images which began in 1972 [4]. Sentinel-2 images have a spatial resolution of up to 10m, while Landsat spectral bands have a resolution of 30m .

The goal of this work is, therefore, to obtain higher resolution images over a longer period of time, and a greater density of images over the years covered simultaneously by Sentinel-2 [3] and Landsat [5, 4] satellites. To do so, we adopt an inverse problem approach to reconstruct high-resolution images from Landsat data (~ 30 m/pixel), **using Sentinel-2 spatial resolution as a (~ 10 m/pixel)** as the spatial resolution reference. More specifically, we develop a

Plug-and-play approach that combines the stability of standard inverse problem formulation and the expressivity of deep neural network models.

Related works - Single image super-resolution is a well known problem in computer vision [6, 7] that has been solved for many years considering variational approaches including the well-known use of total variation (TV) penalization [8] or penalization based on wavelet transform [9]. However, despite the effectiveness of these classical techniques, the ability of deep learning to achieve outstanding restoration quality has driven a shift towards neural networks approaches, where model parameters or priors are now learned directly from data [10, 11]. A wide variety of deep learning frameworks have been made to achieve these tasks [12], starting from supervised model like convolutional neural networks (CNN) based methods [13], to more recent unsupervised approaches using generative adversarial networks (GAN) [14, 15]. Both supervised methods [16, 17, 18], and unsupervised method [19, 20], are able to achieve satisfactory results on super-resolution. However, on the one hand, supervised approaches requires a significant amount of data for their training, which is particularly challenging with remote sensing data, as supervised methods require manually prepared pairs of high- and low-resolution images. Additionally, when handling real satellite data, the pairs of high- and low-resolution images are usually unavailable, because only one satellite image can be acquired at a specific location and time. A common way to handle this problem is to generate low-resolution images using the bicubic interpolation method as a downsampling method [21], but this degradation does not correctly recreate real world low-resolution images [22]. On the other hand, although unsupervised methods have the significant advantage of not requiring high-resolution data for training, their use in remote sensing imagery remains very limited. In addition, the more efficient methods using GANs need to make very strong assumptions about the distribution of data for training the prior, which is not always known on remote sensing images, and this can lead to a deterioration in results and the creation of artifacts [23, 24]. Supervised approaches also involve models other than CNNs, such as Transformers [25]. The term “Transformer” refers to the self-attention mechanism, which models the global relationships among image regions, eliminating the reliance on content-independent convolution kernels used in CNNs. One of the most promising methods in image super-resolution using this approach is SwinIR [26].

Finally, model-based neural network approaches, including unfolded neural networks and Plug-and-Play (PnP) methods, offer a compelling alternative by combining the interpretability of variational methods with the expressiveness of learning-based models, all while requiring fewer parameters. PnP approaches rely on splitting algorithms like forward-backward or ADMM [27] to separate the action of the data fidelity and prior terms. This separation enables the use of learned CNNs as priors without needing pair of low-

and high-resolution. In remote sensing, super-resolution techniques meet a great interest [28, 29], however, model-based neural networks like PnP have been poorly explored. To the best of our knowledge, the only preliminary study was conducted using the U.S. Geological Survey National Map Urban Area imagery collection data [30], focusing on RGB images.

Outline - Section 2 describes the specificities of the considered satellite images, the forward model that establishes the relation between Landsat and Sentinel images, and the adopted PnP strategy with a specific focus on the denoiser. In Section 3, the description of the two datasets considered (synthetic and real) is provided as well as the calibration we made for the forward model. In Section 4, we present a first set of experiments, establishing the behaviour of the proposed PnP w.r.t hyperparameters such as the step-size involved in FB-PnP but also the regularization parameter. We then report the reconstruction results obtained on the two different datasets, along with the evaluation criteria used to compare our main contribution with both a classical interpolation method from the literature and an advanced learning-based approach. Finally, in section 5, we conclude by highlighting the advantages of the PnP method, due to the reduction in data requirements for training and the reduction in training time.

2. PROPOSED METHOD: SPEC-FB-PNP

Data - In this study two sources of data are used. Sentinel-2 images, part of the Copernicus project which started in 2015 [3], and Landsat-8 project which began in 1972 [4]. Sentinel-2 images have a spatial resolution of up to 10m, while Landsat-8 images have a resolution of 30m. Both satellite covers *préciser la couverture spectrale* however in this study we only focus on green, blue, red, and near-infrared bands for their ability to highlight elements of interest in land use and the proximity of their central wavelengths on both data sources. If the reconstruction quality will be of importance in this study, another quantity will also be considered : the normalized water index (NDWI), which highlights water in the images. This index, is calculated from the “green” and “NIR” spectral bands. In the case of Sentinel-2 data (denoted $\mathbf{x} \in \mathbb{R}^{BN}$ where B denotes the number of bands and N the number of pixels), it can be written as follows, for every pixel n ,

$$d_n^{\text{NDWI}} = \frac{X_{\text{green},n} - X_{\text{NIR},n}}{X_{\text{green},n} + X_{\text{NIR},n}}. \quad (1)$$

Forward model - Following [12], we will formulate the forward model as, for every band b ,

$$z_b = (\phi * \bar{x}_b) \downarrow_s + \varepsilon \quad (2)$$

where $\bar{\mathbf{x}} = (\bar{x}_b)_{1 \leq b \leq B} \in \mathbb{R}^{BN}$ denotes the original high resolution (HR) image (i.e., Sentinel-2 image), ϕ denotes the blurring kernel, \downarrow_s the downsampling operator with a decimation factor s , ε the stochastic degradation associated with Gaussian noise, and $\mathbf{z} \in \mathbb{R}^{BM}$ the low-resolution (LR) observation (i.e., Landsat-8).

Our goal is to recover a HR estimate $\hat{\mathbf{x}}$ close from $\bar{\mathbf{x}}$ considering the LR image \mathbf{z} . The long-term goal being to densify the HR observations on the time period where both Landsat-8 and Sentinel-2 images are available (i.e., 2015-now) but also obtain HR images on the period 1972-2015 where only LR Landsat-8 images are available.

In the following, the forward model will be simply formulated as

$$\mathbf{z} = \mathbf{A}\bar{\mathbf{x}} + \varepsilon \quad (3)$$

where \mathbf{A} encodes both the convolution with ϕ and the downsampling \times .

Plug-and-play - The literature of model-based neural network including unfolded neural network and Plug-and-play methods have significantly increased in the past ten years and is now established as good compromise between standard neural networks and variational approaches. Specifically, we investigate the well-established Forward-Backward PnP (FB-PnP) framework. While FB-PnP has been widely studied in general RGB image processing tasks, its use in multispectral imagery remains limited, mainly because it requires the development of a dedicated denoiser capable of handling multi-spectral data.

The iterations of FB-PnP read:

$$\mathbf{x}^{[k+1]} = \mathbf{D}_\theta(\mathbf{x}^{[k]} - \tau \mathbf{A}^\top (\mathbf{A}\mathbf{x}^{[k]} - \mathbf{z}))$$

where $\tau > 0$ is a step-size and \mathbf{D}_θ acts as a denoiser of parameters θ . When $\mathbf{D}_\theta = \text{prox}_{\tau g}$ we recover standard FB schemes and convergence to $\hat{\mathbf{x}} \in \text{Argmin}_x \frac{1}{2} \|\mathbf{A}\mathbf{x} - \mathbf{z}\|_2^2 + g(\mathbf{x})$ is guaranteed for specific choice of τ . Under technical assumptions, in [?] [?], it has been established that the sequence $(\mathbf{x}^{[k]})_{k=0,1,\dots}$ converge to $\hat{\mathbf{x}}$ such that $0 \in \mathbf{A}^\top (\mathbf{A}\hat{\mathbf{x}} - \mathbf{z}) + \mathbf{T}(\hat{\mathbf{x}})$, where \mathbf{T} is related to \mathbf{D}_θ . The involved denoiser should insure specific properties that can be imposed during the training, often at a price of reduced performance.

Building the denoiser - For this work, we choose for the denoiser \mathbf{D}_θ a DRUNet [31], which is a combination of the convolutional network U-Net [32], and the deep residual learning network ResNet [33]. Such a denoiser is available in DeepInverse library [34] but for RGB image denoising. This, to design \mathbf{D}_θ for multispectral image denoising, it was first necessary to change the first and last layers to the source code in order to enable the network to train on 4-channel multispectral data and configure its learning according to specific hyperparameters.

To learn the hyperparameters θ of the proposed denoiser \mathbf{D}_θ , we created a dataset $\mathcal{D} = \{(\bar{\mathbf{x}}^{(\ell)}, \mathbf{y}^{(\ell)})_{\ell=1,\dots,L_D}\}$ such that $\mathbf{y}^{(\ell)} = \bar{\mathbf{x}}^{(\ell)} + \varepsilon$, where $\bar{\mathbf{x}}^{(\ell)}$ denotes the HR Sentinel images and ε a white Gaussian noise with standard deviation σ . These $\bar{\mathbf{x}}^{(\ell)}$ images were obtained using $N = 300 \times 300$ pixels crops of Sentinel-2 images centered on the river corridor of the study area. The study site selected for this work is the Lhasa River in Tibet. This area is of particular interest as it has experienced rapid urbanization in recent years, significantly impacting the development of the alluvial plain and continuing to shape it over time. Sentinel-2 images are acquired over the same area of the Earth’s surface every 5 days, *quelle période de temps ?* The resulting dataset is composed of 1200 image. Few examples extracted from the dataset are displayed in Figure 1.

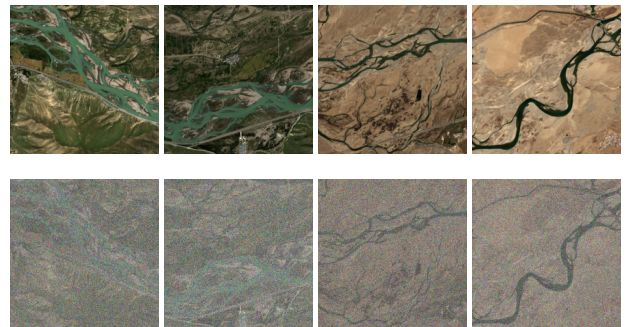


Fig. 1: Comparison of original images $\bar{\mathbf{x}}^{(\ell)}$ and their noisy versions $\mathbf{y}^{(\ell)}$ involving a Gaussian noise with a standard deviation $\sigma = 0.1$.

We consider AdamW optimizer with a learning rate of 0.001. A StepLR scheduler with a step size of 100 and a decay factor of 0.5 was applied, and the network was trained for 1500 epochs. The learning rate and decay factor were chosen based on tests conducted in the Deep Inverse project [34] using three-channel images. To evaluate the impact of the batch size used during the training, two different batch-size have been employed: 4 and 17. In this article, we will only present the reconstruction obtained with a batch-size of 4, given the best results obtained.

3. DATASETS AND FORWARD MODEL CALIBRATION

To evaluate the performance of the FB-PnP method for increasing the resolution of Landsat-8 images to Sentinel-2 images, we consider two types of datasets: a synthetic dataset and a real one. The synthetic one is created to mimic as close as possible the real one but evaluate the performance of our Spec-PnP-FB on a controlled dataset, particularly to verify whether any artifacts are introduced. The interest of evaluating Spec-FB-PnP on the real dataset is to check its stability on a non-ideal situation.

Real dataset and calibration of the forward model - This dataset consists of pairs of Sentinel-2 (\bar{x}_ℓ) and Landsat (z_ℓ^{real}) images, such that $\mathcal{R} = \{(\bar{x}_\ell, z_\ell^{\text{real}})_{\ell=\{1, \dots, L_R\}}\}$. The underlying forward model is of the form (2) where ϕ , s and ε are estimated from the data. It is also important to notice that because these data come from different sources, it was not possible to obtain acquisitions that were spatially aligned on the same location and at the same time. To overcome these constraints, after downloading the images from the two sources, we classified them chronologically in order to create $\{(\bar{x}_\ell, z_\ell^{\text{real}})\}$ image pairs that were as close as possible in their acquisition time. For spatial alignment, it was possible to use Landsat data from the Harmonized Landsat Sentinel-2 (HLS) project [5], which reprojected Landsat images onto the Sentinel-2 UTM tiling grid.

The \bar{x}_ℓ images were obtained by cropping Sentinel-2 images of size 11000×11000 px using a $N = 300 \times 300$ pixels window, focusing the extraction on the river corridor using the associated centerline obtained from the Global Surface Water (GSW) dataset [35]. The same procedure was used on Landsat images of size 3660×3660 px using a $M = 100 \times 100$ pixels window.

This difference in window size is due to the scale factor $s = 3$, Sentinel-2 images, which have a 10m spatial resolution, and Landsat images, which have a 30m spatial resolution. The blurring kernel ϕ with a standard deviation $\sigma = 0.1$ and a size of 4×4 px, has been calibrated by taking into account concepts from the literature for the choice of kernel width [36] and from $(\bar{x}_\ell, z_\ell^{\text{real}})$ in order to minimize the error $\|(\phi * \bar{x}_\ell - z_\ell^{\text{real}}) \downarrow_s\|_2^2$. The standard deviation of white Gaussian noise, was estimated using the median absolute deviation (MAD) technique. This method consists of performing a wavelet decomposition of a Landsat image to obtain the wavelet details coefficients such that: $\sigma \approx \frac{\text{median}(|W_{z_\ell^{\text{real}}}|)}{0.6745}$ [?].

Synthetic dataset - This second dataset has been defined to validate the Spec-FB-PnP on data for which ground truth is available. The dataset is $\mathcal{S} = \{(\bar{x}_\ell, z_\ell^{\text{synt}})_{\ell=\{1, \dots, L_S\}}\}$ with $z_\ell^{\text{synt}} = (\phi * \bar{x}_\ell) \downarrow_s + \varepsilon$ where ϕ and ε are calibrated from the real Landsat images z_ℓ^{real} as described in the paragraph above.

4. NUMERICAL EXPERIMENT

Evaluation criteria - The PSNR was used as the main indicator. Then, evaluate the robustness of the model in reconstructing intensity dynamics, a spectral index specific for highlighting the presence

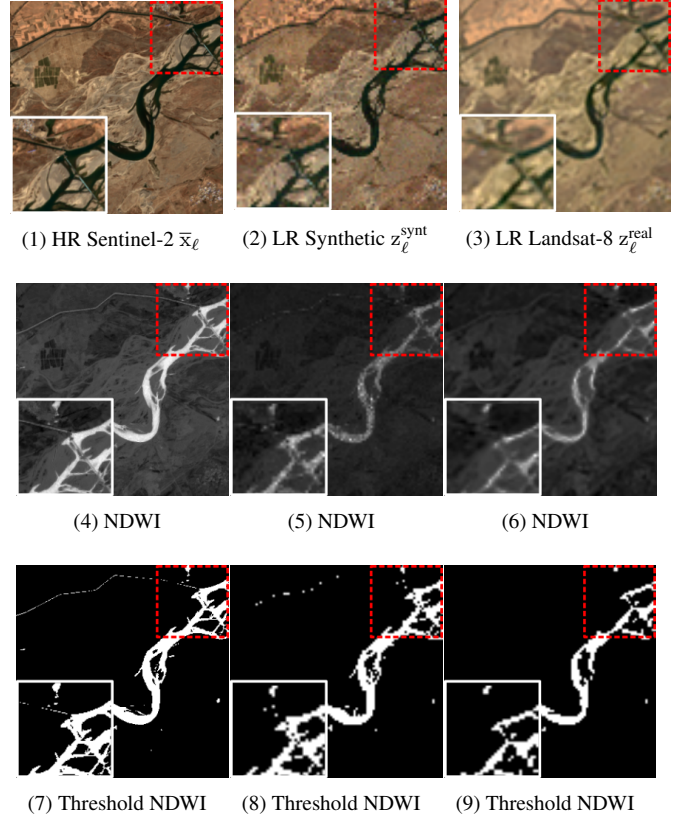


Fig. 2: Line 1 - RGB reference, Line 2 - NDWI reference, Line 3 - threshold of NDWI index, **Problème dans l’affichage, mettre tabular + ajouter légende**

of water, the Normalized Difference Water Index (NDWI) (Figure 2), was calculated on the reconstruction. This spectral indicator allows extracting hydromorphological metrics, such as the river perimeter or the surface area of open water, and comparing them with the values obtained from high-resolution reference images.

The reconstructions obtained with the Plug-and-Play method were compared with those from the bicubic interpolation implemented in PyTorch, as well as a novel learning-based method named SwinIR [26]. This second methodology was trained on the same dataset as the DRUNet, with the same number of epochs (1500). Tables 1 present the indicators extracted from the reconstructions obtained using the different methods, based on the real Landsat images and the synthetic Landsat images generated from Sentinel-2 data. The tables also report the water area values for the reference images, as well as for the two example observations, respectively. **Impact of the step-size and regularization parameter in PnP** - As observed from our results, a larger batch size during training can result in the loss of fine details in high-resolution image reconstructions compared to a smaller batch size. We also note that some artifacts may appear in more homogeneous areas, however, despite this, the reconstructions maintain strong spatial coherence across most of the water bodies, which are the most critical elements for evaluating changes in hydromorphology over time.

Comments on reconstruction performance -

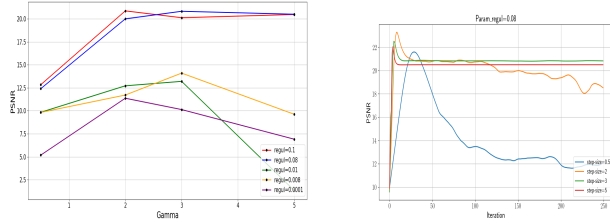


Fig. 3: Caption

Reconstruction image A	SSIM	PSNR	Water area
Reference image A			22 580 m ²
Landsat synth A			8 730 m ²
Bicubic interpolation	0.59	22.7	21 340 m ²
SwinIR	0.87	30.0	21 980 m ²
P&P 4	0.88	28.4	22 620 m²
Landsat real A			4740 m ²
Bicubic interpolation	0.51	19.1	15 730 m ²
SwinIR	0.65	20.3	16 600 m²
P&P 4	0.60	19.5	15 510 m ²
Sentinel B			26 620 m ²
Landsat synth B			7 290 m ²
Bicubic interpolation	0.62	24.2	26 310 m²
SwinIR	0.85	30.8	24 880 m ²
P&P 4	0.82	27.6	23 670 m ²
Landat real B			7110 m ²
Bicubic	0.53	14.73	21 920 m²
SwinIR	0.60	14.94	19 010 m ²
P&P 4	0.64	15.03	20 530 m ²

Table 1: Metrics of the reconstruction of Image A and B

5. CONCLUSION

6. ACKNOWLEDGEMENTS

This work is funded as part of ANR GloUrb project (ANR-22-CE03-0005). The project is also co-financed by the Labex IMU (ANR-10-LABEX-0088) and the EUR H2O'Lyon (ANR-17-EURE-0018) of the University of Lyon, as part of the "Investissements d'Avenir" programme operated by the ANR.

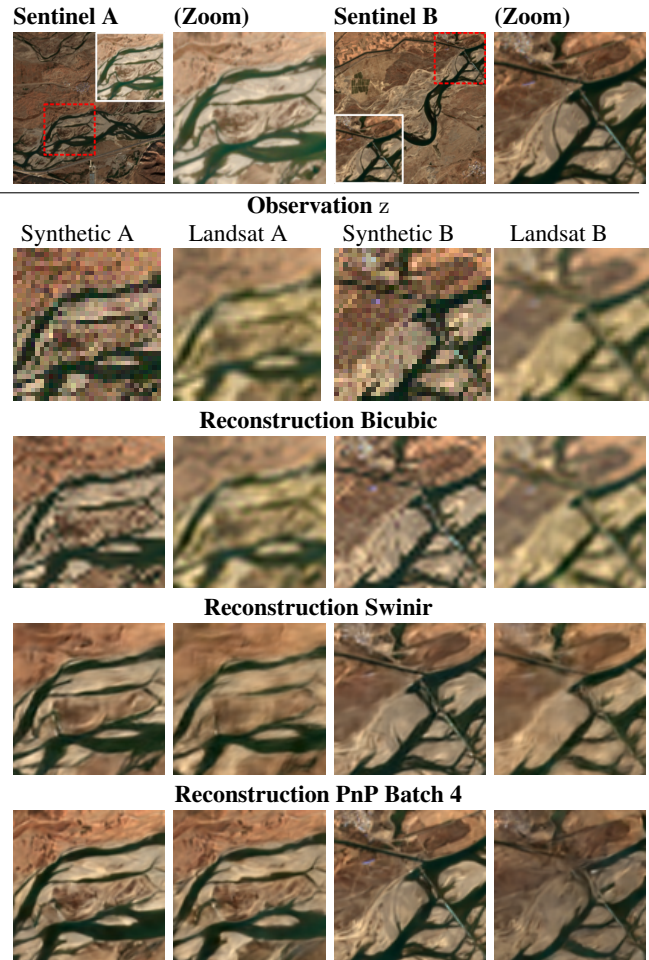


Fig. 4: TO ADD

7. REFERENCES

- [1] H. M. Habersack, "The river-scaling concept (rsc): a basis for ecological assessments," *Hydrobiologia*, vol. 422, no. 0, pp. 49–60, 2000.
- [2] P. J. Crutzen, "The "Anthropocene";" *Journal de Physique IV (Proceedings)*, 2002.
- [3] F. Gascon, E. Cadau, O. Colin, B. Hoersch, C. Isola, B. L. Fernandez, and P. Martimort, "Copernicus sentinel-2 mission: products, algorithms and cal/val," in *Earth observing systems XIX*. SPIE, 2014, vol. 9218, pp. 455–463.
- [4] M. A. Wulder, T. R. Loveland, D. P. Roy, C. J. Crawford, J. G. Masek, C. E. Woodcock, R. G. Allen, M. C. Anderson, A. S. Belward, and W. B. Cohen, "Current status of landsat program, science, and applications," *Remote Sensing of Environment*, vol. 225, pp. 127–147, 2019.
- [5] M. Claverie, J. Ju, J. G. Masek, J. L. Dungan, E. F. Vermote, J.-C. Roger, S. V. Skakun, and C. Justice, "The harmonized landsat and sentinel-2 surface reflectance data set," *Remote Sensing of Environment*, vol. 219, pp. 145–161, 2018.
- [6] M. Irani and S. Peleg, "Improving resolution by image reg-

- istration,” *CVGIP: Graphical Models and Image Processing*, vol. 53, no. 3, pp. 231–239, 1991.
- [7] W. T. Freeman, E. C. Pasztor, and O. T. Carmichael, “Learning low-level vision,” *International Journal of Computer Vision*, vol. 40, no. 1, pp. 25–47, 2000.
- [8] S. D. Babacan, R. Molina, and A. K. Katsaggelos, “Variational bayesian super resolution,” *IEEE Transactions on Image Processing*, vol. 20, no. 4, pp. 984–999, 2010.
- [9] H. Ji and C. Fermüller, “Robust wavelet-based super-resolution reconstruction: theory and algorithm,” *IEEE Transactions on Pattern Analysis and Machine Intelligence*, vol. 31, no. 4, pp. 649–660, 2008.
- [10] M. Nazzal and H. Ozkaramanli, “Wavelet domain dictionary learning-based single image superresolution,” *Signal, Image and Video Processing*, vol. 9, no. 7, pp. 1491–1501, 2015.
- [11] F. Deeba, S. Kun, F. A. Dharejo, and Y. Zhou, “Wavelet-based enhanced medical image super resolution,” *IEEE Access*, vol. 8, pp. 37035–37044, 2020.
- [12] Z. Wang, J. Chen, and S. C. H. Hoi, “Deep learning for image super-resolution: A survey,” *IEEE Transactions on Pattern Analysis and Machine Intelligence*, vol. 43, no. 10, pp. 3365–3387, 2020.
- [13] C. Dong, C. C. Loy, K. He, and X. Tang, “Learning a deep convolutional network for image super-resolution,” in *European conference on computer vision*. Springer, 2014, pp. 184–199.
- [14] C. Ledig, L. Theis, F. Huszár, J. Caballero, A. Cunningham, A. Acosta, A. Aitken, A. Tejani, J. Totz, and Z. Wang, “Photo-realistic single image super-resolution using a generative adversarial network,” in *Proceedings of the IEEE conference on computer vision and pattern recognition*, 2017, pp. 4681–4690.
- [15] I. Goodfellow, J. Pouget-Abadie, M. Mirza, B. Xu, D. Warde-Farley, S. Ozair, A. Courville, and Y. Bengio, “Generative adversarial nets,” *Advances in Neural Information Processing Systems*, vol. 27, 2014.
- [16] J. Wang, Y. Wu, L. Wang, L. Wang, O. Alfarraj, and A. Tolba, “Lightweight feedback convolution neural network for remote sensing images super-resolution,” *IEEE Access*, vol. 9, pp. 15992–16003, 2021.
- [17] C. Ren, X. He, L. Qing, Y. Wu, and Y. Pu, “Remote sensing image recovery via enhanced residual learning and dual-luminance scheme,” *Knowledge-Based Systems*, vol. 222, pp. 107013, 2021.
- [18] F. Deeba, F. A. Dharejo, Y. Zhou, A. Ghaffar, M. H. Memon, and S. Kun, “Single image super-resolution with application to remote-sensing image,” in *2020 Global Conference on Wireless and Optical Technologies (GCWOT)*. IEEE, 2020, pp. 1–6.
- [19] K. Prajapati, V. Chudasama, H. Patel, K. Upla, R. Ramachandra, K. Raja, and C. Busch, “Unsupervised single image super-resolution network (usisresnet) for real-world data using generative adversarial network,” in *Proceedings of the IEEE/CVF Conference on Computer Vision and Pattern Recognition Workshops*, 2020, pp. 464–465.
- [20] G. Kim, J. Park, K. Lee, J. Lee, J. Min, B. Lee, D. K. Han, and H. Ko, “Unsupervised real-world super resolution with cycle generative adversarial network and domain discriminator,” in *Proceedings of the IEEE/CVF Conference on Computer Vision and Pattern Recognition Workshops*, 2020, pp. 456–457.
- [21] C. Tuna, G. Unal, and E. Sertel, “Single-frame super resolution of remote-sensing images by convolutional neural networks,” *International Journal of Remote Sensing*, vol. 39, no. 8, pp. 2463–2479, 2018.
- [22] J. Gu, H. Lu, W. Zuo, and C. Dong, “Blind super-resolution with iterative kernel correction,” in *Proceedings of the IEEE/CVF Conference on Computer Vision and Pattern Recognition*, 2019, pp. 1604–1613.
- [23] M. Daniels, P. Hand, and R. Heckel, “Reducing the representation error of gan image priors using the deep decoder,” *arXiv preprint arXiv:2001.08747*, 2020.
- [24] R. Mechrez, I. Talmi, F. Shama, and L. Zelnik-Manor, “Maintaining natural image statistics with the contextual loss,” in *Asian Conference on Computer Vision*. Springer, 2018, pp. 427–443.
- [25] Ashish Vaswani, Noam Shazeer, Niki Parmar, Jakob Uszkoreit, Llion Jones, Aidan N Gomez, Łukasz Kaiser, and Illia Polosukhin, “Attention is all you need,” *Advances in neural information processing systems*, vol. 30, 2017.
- [26] J. Liang, J. Cao, G. Sun, K. Zhang, L. Van Gool, and R. Timofte, “Swinir: Image restoration using swin transformer,” in *Proceedings of the IEEE/CVF International Conference on Computer Vision*, 2021, pp. 1833–1844.
- [27] S. V. Venkatakrishnan, C. A. Bouman, and B. Wohlberg, “Plug-and-play priors for model-based reconstruction,” in *IEEE Glob. Conf. Signal Inf. Process. Proc.*, Austin, TX, USA, 2013, pp. 945–948.
- [28] P. Wang, B. Bayram, and E. Sertel, “A comprehensive review on deep learning based remote sensing image super-resolution methods,” *Earth-Science Reviews*, vol. 232, pp. 104110, 2022.
- [29] W. Yang, X. Zhang, Y. Tian, W. Wang, J.-H. Xue, and Q. Liao, “Deep learning for single image super-resolution: A brief review,” *IEEE Transactions on Multimedia*, vol. 21, no. 12, pp. 3106–3121, 2019.
- [30] H. Tao, “Super-resolution of remote sensing images based on a deep plug-and-play framework,” in *IGARSS 2020-2020 IEEE International Geoscience and Remote Sensing Symposium*. IEEE, 2020, pp. 625–628.
- [31] K. Zhang, Y. Li, W. Zuo, L. Zhang, L. Van Gool, and R. Timofte, “Plug-and-play image restoration with deep denoiser prior,” *IEEE Transactions on Pattern Analysis and Machine Intelligence*, vol. 44, no. 10, pp. 6360–6376, 2021.
- [32] O. Ronneberger, P. Fischer, and T. Brox, “U-net: Convolutional networks for biomedical image segmentation,” in *International Conference on Medical image computing and computer-assisted intervention*. Springer, 2015, pp. 234–241.
- [33] K. He, X. Zhang, S. Ren, and J. Sun, “Deep residual learning for image recognition,” in *Proceedings of the IEEE conference on computer vision and pattern recognition*, 2016, pp. 770–778.
- [34] J. Tachella, M. Terris, S. Hurault, A. Wang, D. Chen, M.-H. Nguyen, M. Song, T. Davies, L. Davy, J. Dong, P. Escande, J. Hertrich, Z. Hu, T. I. Liaudat, N. Laurent, B. Levac, M. Massias, T. Moreau, T. Modrzyk, B. Monroy, S. Neumayer, J. Scanvic, F. Sarron, V. Sechaud, G. Schramm, R. Vo, and P. Weiss, “Deepinverse: A python package for solving imaging inverse problems with deep learning,” 2025.

- [35] J.-F. Pekel, A. Cottam, N. Gorelick, and A. S. Belward, “High-resolution mapping of global surface water and its long-term changes,” *Nature*, vol. 540, no. 7633, pp. 418–422, 2016.
- [36] N. Efrat, D. Glasner, A. Apartsin, B. Nadler, and A. Levin, “Accurate blur models vs. image priors in single image super-resolution,” in *Proceedings of the IEEE International Conference on Computer Vision*, 2013, pp. 2832–2839.